Finite-Size Effect in Phonon-Induced Elliott-Yafet Spin Relaxation in Al

J. D. Watts[1,2] J. T. Batley,[2] N. A. Rabideau[2] J. P. Hoch[2] L. O'Brien[2,3] P. A. Crowell,[1] and C. Leighton[2,*]

[1]*School of Physics and Astronomy, University of Minnesota, Minneapolis, Minnesota 55455, USA*
[2]*Department of Chemical Engineering and Materials Science, University of Minnesota, Minneapolis, Minnesota 55455, USA*
[3]*Department of Physics, University of Liverpool, Liverpool L69 3BX, United Kingdom*

The Elliott-Yafet theory of spin relaxation in nonmagnetic metals predicts proportionality between spin and momentum relaxation times for scattering centers such as phonons. Here, we test this theory in Al nanowires over a very large thickness range (8.5–300 nm), finding that the Elliott-Yafet proportionality "constant" for phonon scattering in fact exhibits a large, unanticipated finite-size effect. Supported by analytical and numerical modeling, we explain this *via* strong phonon-induced spin relaxation at surfaces and interfaces, driven in particular by enhanced spin-orbit coupling.

The relaxation of electron spins in nonmagnetic (N) metals after injection from ferromagnetic (F) materials is foundational in spintronics, impacting spin valves, spin pumping, spin torques, etc. [1–4]. In light metals, the Elliott-Yafet (EY) mechanism is understood to control this process, leading to $\tau_s = \beta\tau_e$, where τ_s is the spin lifetime [related to the spin diffusion length and diffusivity *via* $\lambda_N = (D\tau_s)^{1/2}$] and τ_e is the momentum relaxation time [5,6]. The EY constant $\beta = (\Delta E/\lambda_{\text{SO}})^2$ is thus an inverse probability of spin relaxation per scattering event, with ΔE being the energy difference between bands involved in scattering and λ_{SO} the spin-orbit coupling [5–8]. In real materials, multiple scattering sources lead to a generalized EY relation $\tau_s^{-1} = \sum_i \beta_i^{-1}\tau_{e,i}^{-1}$, where the spin relaxation rate is expressed in terms of momentum relaxation rates at each scattering source ($\tau_{e,i}^{-1}$) and their individual β_i [9–12]. The β_i for phonons and common defects (grain boundaries, point defects, etc.) are poorly understood, however, even in simple N metals, significantly limiting this approach [9–12].

Understanding of EY spin relaxation is progressing, however, particularly in nonlocal spin valves (NLSVs) [13,14]. In these devices, spins are injected from a F contact into a N nanowire, then diffuse a lateral distance d, before detection at a second F through a nonlocal resistance. Vitally, NLSVs generate pure, diffusive spin currents [13–15], minimizing artifacts and enabling reliable extraction of $\tau_s(T)$ and $\tau_e(T)$, and thus EY constants [9–12,16–23]. In Cu films, for example, the β_i for phonon scattering ($\beta_{\text{ph}} \approx 750$) has been separated from the β_i for defects (β_{def}), β_{def} being subsequently decomposed into grain boundary and magnetic impurity components ($\beta_{\text{GB}} \approx 250$ and $\beta_K \approx 1.5$) [12]. The latter was enabled by the discovery of a spin-transport Kondo effect [24], in which, remarkably, spin relaxation at magnetic impurities

can also be cast in EY form [25]. The extremely low β_K in Cu, however ($\sim$500 times smaller than β_{ph}), i.e., the extraordinary efficiency of Kondo spin relaxation, means that even part-per-million-level magnetic impurities obscure other spin relaxation processes [12,20,24,26,27].

Because of low Z and negligible Kondo effects [24,28], Al is highly attractive for metallic spin relaxation studies. We refer here to the fact that Al does not support local moments on dilute transition-metal impurities, eliminating spin relaxation due to Kondo scattering [24,28]. Remarkably, however, β_{ph} in polyvalent metals such as Al and Mg is orders of magnitude beneath EY predictions, evading understanding for $\sim$40 yr [6,29]. Fabian and Das Sarma addressed this by noting that large Fermi surfaces in polyvalent metals inevitably cross Brillouin zone boundaries, special symmetry points, and other degeneracy lines, creating momentum-space regions where $\Delta E \to 0$ and spin relaxation rates diverge [30,31]. Fermi surface "hot spots" thus dominate spin relaxation in Al, calculations with sufficient accuracy to achieve agreement with experiment on β_{ph} emerging only in the 1990s [30,31]. For $\sim$20 yr, phonon-mediated EY spin relaxation in this model elemental metal has therefore appeared to be understood. Experimental characterization of phonon-induced spin relaxation in Al is surprisingly limited, however. NLSV determinations of β_{ph} often hinge on only 300 and $\sim$4.2 K data points [11,32], defect-induced spin relaxation is often emphasized over phonon-induced relaxation [9,10], and historical conduction electron spin resonance (CESR) data are limited to <100 K [7,29,33].

Here, we provide extensive T-dependent measurements of τ_s and λ_N in Al NLSVs, thus determining β_{ph} over a previously unexplored range of N film thickness (t_N), from 8.5–300 nm. Remarkably, β_{ph} is *not* constant; it in fact decreases from $\sim$26 000 in the high-t_N limit to as low as

~ 1000 at $t_N \approx 10$ nm, revealing a prominent, unanticipated finite-size effect. Related t_N dependence is found in the Debye temperature (θ_D) from T-dependent resistivity, implicating lattice softening and surface or interface effects. We proceed to develop analytical and numerical models demonstrating that reduced surface or interface β_{ph} of ~ 600, applied within only ~ 0.5 nm of the surface or interface, quantitatively reproduces experimental data. We thus deduce strong phonon-induced spin relaxation at surfaces or interfaces, driven in particular by enhanced λ_{SO}. In addition to uncovering a broadly significant phenomenon, these results impact spintronic devices. NLSV-based spin accumulation sensors, for example, are contenders for next-generation hard drive read heads [34–36], but require $t_N < 10$ nm, where our findings substantially modify performance predictions.

Figure 1(a) shows a scanning electron microscopy (SEM) image of a representative Co/Al NLSV, fabricated
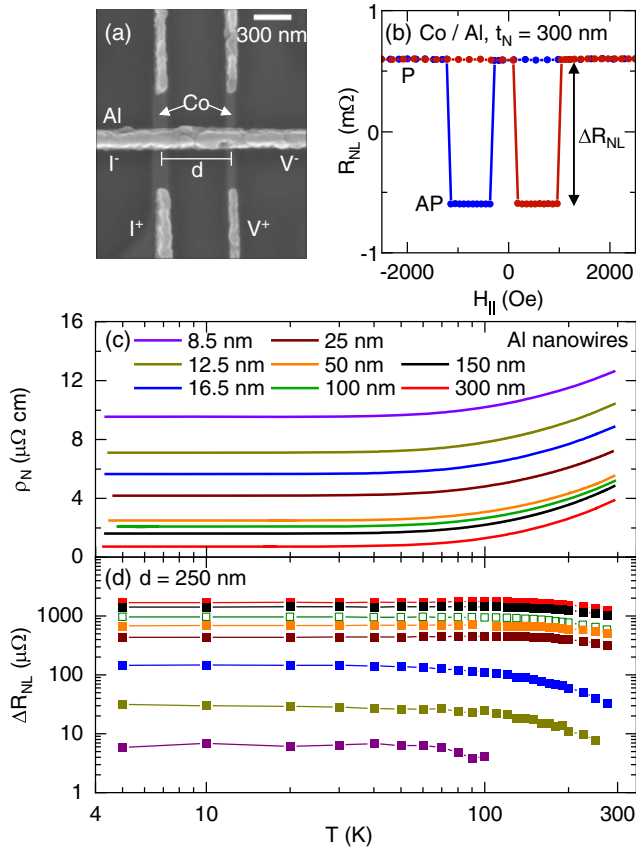

FIG. 1. (a) SEM image of a Co/Al NLSV illustrating the measurement configuration (I,V denote current and voltage). (b) Representative background-subtracted [40] R_{NL} vs H for a Co/Al NLSV with $t_N = 300$ nm, $d = 500$ nm, at 5 K. Red and blue denote different sweep directions. (c) T dependence (linear-$\log_{10}$ scale) of ρ_N for Al nanowires with $t_N = 8.5$–300 nm. (d) T dependence of ΔR_{NL} ($\log_{10}$-$\log_{10}$ scale) for Co/Al NLSVs with the same t_N (and color scheme); all data are for $d = 250$ nm, except $t_N = 100$ nm (open points), for which $d = 500$ nm.

(and measured) via methods described in Supplemental Material, Sec. A [37]. Briefly, a charge current I is injected from one F Co contact into the N Al channel, generating a nonequilibrium spin population and a pure, diffusive spin current between the F's. A nonlocal voltage V_{NL} is then detected between the channel and the second F, leading to a nonlocal resistance $R_{\mathrm{NL}} = V_{\mathrm{NL}}/I$, shown vs magnetic field (H) in Fig. 1(b). The two F's have differing coercivities, enabling toggling between parallel (P) and antiparallel (AP) magnetizations, the resulting ΔR_{NL} [Fig. 1(b)] being a direct measure of the spin population at distance d. Measurements of $\Delta R_{\mathrm{NL}}(d)$ thereby determine λ_N and τ_s.

The NLSVs here have similar dimensions for the F Co contacts (Supplemental Material, Sec. A [37]), but Al channels with t_N from 8.5–300 nm. (At low t_N we report thicknesses after accounting for oxidation of ~ 1.5 nm of Al; the channels are thus capped with AlO_x, while the bottom interface is with Si/Si-N). Figure 1(c) shows the t_N evolution of the T-dependent N resistivity [$\rho_N(T)$]. $\rho_N(T)$ shifts uniformly upwards with decreasing t_N, indicating increasing residual resistivity ρ_0, as expected from grain size reduction, surface/interface scattering, etc. [41,42]. ρ_0 in fact increases over tenfold, from 0.7 to 9.5 $\mu\Omega$ cm, while the phonon contribution to ρ_N remains almost constant. Figure 1(d) shows the impact on $\Delta R_{\mathrm{NL}}(T)$ at an illustrative $d = 250$ nm. At high t_N (e.g., 300 nm), ΔR_{NL} approaches 2 mΩ, is flat at low T (confirming Kondo effects are absent [24]), and rolls off at high T. This occurs due to increased ρ_N at higher T, and thus decreased τ_e and τ_s. As t_N is decreased, $\Delta R_{\mathrm{NL}}(T \to 0)$ decreases by ~ 300 times, reflecting the defect-induced spin relaxation we will discuss elsewhere [43]; we focus here on phonon-induced EY spin relaxation. The latter also evolves with t_N, as illustrated by the noticeably different $\Delta R_{\mathrm{NL}}(T)$ for $t_N \leq 16.5$ nm. At the highest T and lowest t_N, ΔR_{NL} falls to a few $\mu\Omega$, reaching our noise floor.

As shown in Figs. 2(a) and 2(b) for illustrative t_N of 300 and 16.5 nm, $\Delta R_{\mathrm{NL}}(d)$ measurements at various T enable extraction of $\lambda_N(T)$ via fitting to the Takahashi-Maekawa formula [15] based on Valet-Fert theory (solid lines) [44], under the (verified [24,27,45]) assumption of transparent F/N interfaces. Details are provided in Supplemental Material, Sec. B [37], but we note that all dimensions and the F resistivity are directly measured, and the F spin diffusion length is accounted for via resistivity scaling [12,18,24,26,27,45,46]. Only the spin polarization (α) and λ_N remain as fitting parameters, and these are independent as the Takahashi-Maekawa formula reduces to $\exp(-d/\lambda_N)$ at high d [see the straight-line behavior on the $\log_{10}$-linear plots in Figs. 2(a) and 2(b)]. The resulting $\lambda_N(T)$ are shown in Fig. 2(c). At high t_N (e.g., 300 nm), λ_N increases substantially on cooling, from ~ 600 nm at 275 K to ~ 1500 nm at low T, before saturating. This is *qualitatively* consistent with EY spin relaxation: As $\rho_N(T)$ decreases on cooling [Fig. 1(c)], $\tau_e(T)$ grows and saturates, meaning that
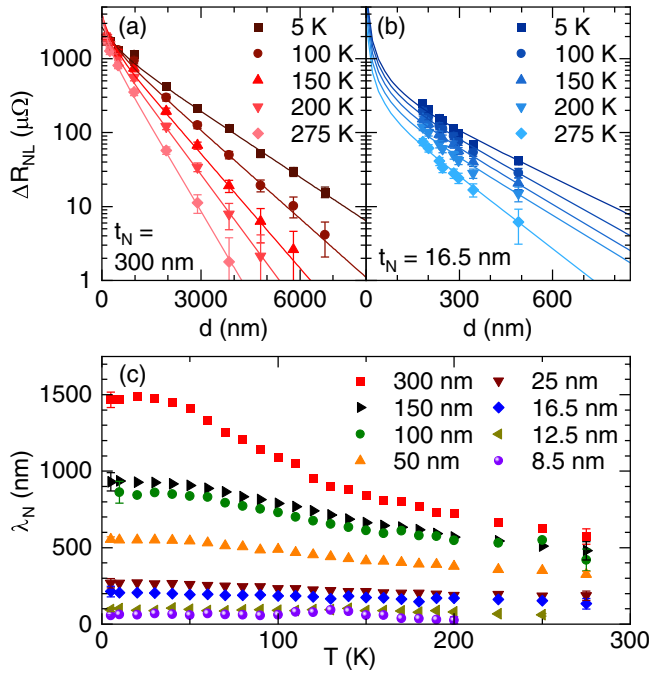
FIG. 2. (a),(b) $\Delta R_{\rm NL}(d)$ vs T for Co/Al NLSVs with $t_N = 300$ and 16.5 nm. Solid lines are Takahashi-Maekawa fits [15]. (c) T dependence of λ_N for t_N from 8.5 to 300 nm. Representative uncertainties are shown on first and last points.

$\tau_s(T)$ and $\lambda_N(T)$ should also. Also *qualitatively* consistent with EY relaxation, as t_N is decreased, $\lambda_N(T \to 0)$ decreases, λ_N eventually becoming notably T independent at the lowest t_N.

Quantitative testing of EY behavior was done by extracting $\tau_e(T)$ from $\rho_N(T)$ [Fig. 1(c)] using $\tau_e(T) = 3D(T)/v_F^2$ (where $v_F = 2.03 \times 10^6$ ms^{-1} is the Al Fermi velocity), and $D(T) = [N(E_F)e^2\rho_N(T)]^{-1}$ [where $N(E_F) = 2.4 \times 10^{28}$ eV^{-1} m^{-3} is the density of states at the Fermi level and e is the electronic charge] [47]. $\lambda_N(T)$ [Fig. 2(c)] is then converted to $\tau_s(T) = \lambda_N^2(T)/D(T)$, enabling direct comparison of $\tau_s(T)$ and $\tau_e(T)$ (see Supplemental Material, Sec. C [37]). This is done using the generalized EY relation to separate phonon and defect (T-independent) contributions, writing

$$\tau_s^{-1}(T) = \beta_{\rm ph}^{-1}\tau_{e,\rm ph}^{-1}(T) + \beta_{\rm def}^{-1}\tau_{e,\rm def}^{-1}, \qquad (1)$$

where $\tau_{e,\rm ph}^{-1}(T)$ and $\tau_{e,\rm def}^{-1}$ are phonon and defect contributions to the momentum relaxation rate [9–12,16–23]. As in Fig. 3(a), τ_s^{-1} can thus be plotted vs $\tau_{e,\rm ph}^{-1}$ with T as the implicit variable (higher T increases $\tau_{e,\rm ph}^{-1}$) [12,22]. Fits to Eq. (1) [solid lines in Fig. 3(a)], thus yield $\beta_{\rm ph}^{-1}$ as the slope and $\beta_{\rm def}^{-1}\tau_{e,\rm def}^{-1}$ as the intercept. Equation (1) indeed describes the data at all t_N (no low-T deviation occurs, again ruling out Kondo relaxation [12]), with τ_s^{-1} increasing as t_N is decreased. Focusing on phonon-induced spin relaxation,
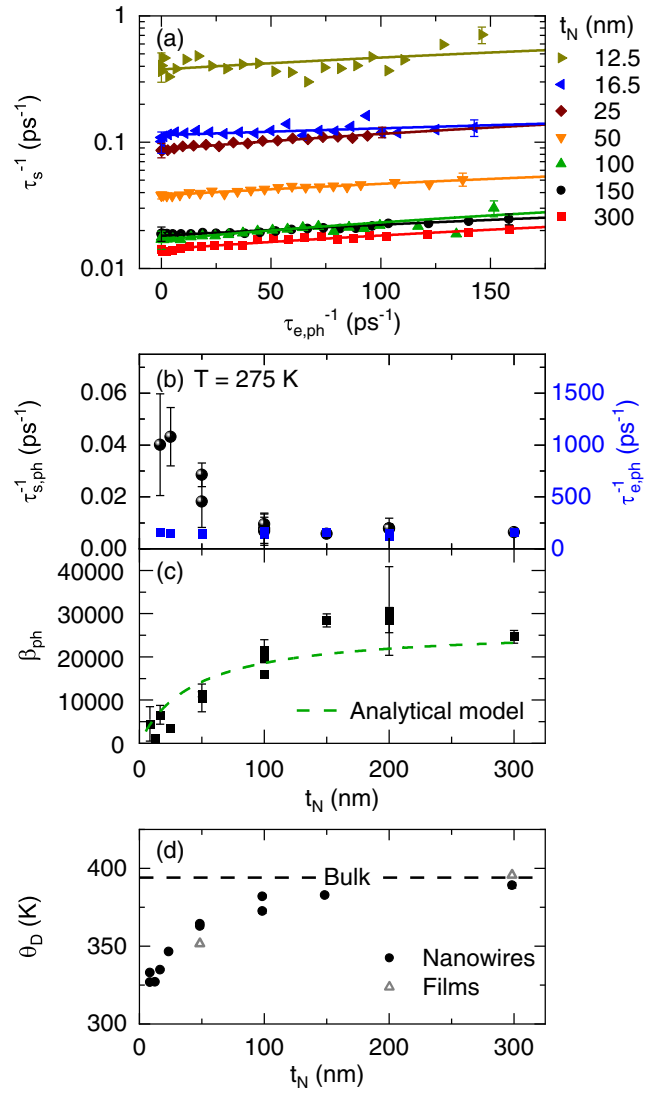

FIG. 3. (a) τ_s^{-1} vs $\tau_{e,\rm ph}^{-1}$ from Co/Al NLSVs with t_N from 12.5 to 300 nm (8.5 nm data were excluded due to lack of data significantly above the noise at high T [see Fig. 1(d), Supplemental Material, Sec. F [37]]. Solid lines are fits to Eq. (1). (b) 275-K t_N dependence of $\tau_{s,\rm ph}^{-1}$ (black, left axis) and $\tau_{e,\rm ph}^{-1}$ (blue, right axis), with the axis scales chosen such that points coincide at high t_N. (c) t_N dependence of $\beta_{\rm ph}$; the green dashed line is a fit to Eq. (2). (d) t_N dependence of θ_D from $\rho_N(T)$ of Al nanowires and films (open points); the bulk θ_D is marked. In (b)–(d) multiple points are plotted at some t_N, from repeat devices.

Fig. 3(b) shows the t_N dependence of the 275-K $\tau_{s,\rm ph}^{-1}$ (left axis) and $\tau_{e,\rm ph}^{-1}$ (right axis). As discussed with Fig. 1(c), $\tau_{e,\rm ph}^{-1}$ is essentially constant (see Supplemental Material, Sec. C [37]). $\tau_{s,\rm ph}^{-1}$, however, is not at all constant. It increases from $\sim$0.006 ps^{-1} at $t_N = 300$ nm, to $\sim$0.04 ps^{-1} at $t_N \approx 10$ nm, i.e., by $\sim$10 times, particularly below $\sim$100 nm. As $\beta_{\rm ph}$ is the proportionality constant between these two rates, clearly, the EY "constant" for phonon scattering is actually size dependent.

Figure 3(c) reinforces the above by plotting β_{ph} vs t_N. At high t_N, e.g., $t_N \geq 150$ nm, β_{ph} is approximately constant, the error-weighted average being 26 000. This is within a factor of 2 of the "hot spot" calculation of Fabian and Das Sarma ($\beta_{ph} = 12\,500$) [30], but 3–6 times above CESR estimates, although those were determined below $\sim$100 K [33,48]. At lower t_N in Fig. 3(c), however, β_{ph} decreases, reaching $\sim$11 000 at $t_N = 50$ nm, in good agreement with the 12 600 and 13 200 from other Al NLSVs at this t_N [11,32,49]. Further decreases occur below this, β_{ph} eventually reaching $\sim$1000 at $t_N = 12.5$ nm. The full variation in β_{ph} is thus a factor of 26, i.e., a 26-fold increase in phonon-induced spin relaxation probability as t_N decreases from 300 to $\sim$10 nm. This is not readily visible in Fig. 3(a) due to the $\log_{10}$ scale and large variation in intercept (due to defect-induced spin relaxation [43]), but is striking in Figs. 3(b) and 3(c).

Hints to the origin of this effect are provided by Fig. 3(d), which shows the t_N dependence of θ_D extracted from Bloch-Grüneisen analysis of $\rho_N(T)$ (Supplemental Material, Sec. D [37]). Comparing Figs. 3(c) and 3(d), θ_D decreases on a similar length scale to β_{ph}, specifically below $t_N \approx 100 - 150$ nm. This is the well-known lattice softening effect in metallic films and nanowires [50–52], immediately suggesting a role for surfaces or interfaces in the t_N dependence of β_{ph}. Specifically, we propose that metallic spin relaxation induced by phonons at surfaces or interfaces is distinctly different from that induced by bulk phonons. We test this via a simple analytical model in which an effective β_{ph} ($\beta_{ph,eff}$) is expressed in terms of $\beta_{ph,bulk}$ in the Al interior [constrained to 26 000 from Fig. 3(c)] and a smaller $\beta_{ph,surf}$ applied only within t_{surf} of the surface or interface. A thickness-weighted average then yields

$$\beta_{ph,eff} = \frac{\tau_{e,ph}^{-1}}{\tau_{s,ph,eff}^{-1}} = \frac{\tau_{e,ph}^{-1}}{\left(\frac{t_N - 2t_{surf}}{t_N}\right)\tau_{s,ph,bulk}^{-1} + \left(\frac{2t_{surf}}{t_N}\right)\tau_{s,ph,surf}^{-1}}, \quad (2)$$

where $\tau_{s,ph,eff}^{-1}$ is the effective spin relaxation rate due to phonon scattering and $\tau_{s,ph,bulk}^{-1}$ and $\tau_{s,ph,surf}^{-1}$ are related to $\tau_{e,ph}^{-1}$ [$\sim$160 ps^{-1} from Fig. 3(b)] via $\beta_{ph,bulk}$ and $\beta_{ph,surf}$. The data of Fig. 3(c) can then be fit with Eq. (2) with $\beta_{ph,surf}$ as the only parameter, provided t_{surf} is fixed. We set t_{surf} by noting that both the length scale for surface structural relaxation in Al [53], and the Debye wavelength ($\lambda_D = h v_s / k_B \theta_D$, where $\theta_D = 394$ K and the phonon velocity for the relevant acoustic modes $v_s = 4.2$ km s^{-1}) [54,55], are $\sim$0.5 nm. We thus set $t_{surf} = 0.5$ nm in Eq. (2) as a simple estimate of the length scale over which β_{ph} could be surface or interface modified, resulting in the green dashed line fit in Fig. 3(c), where $\beta_{ph,surf} = 600$, i.e., $\sim$40 times smaller than bulk. The fit is reasonable, demonstrating that imposing lower $\beta_{ph,surf}$ within only
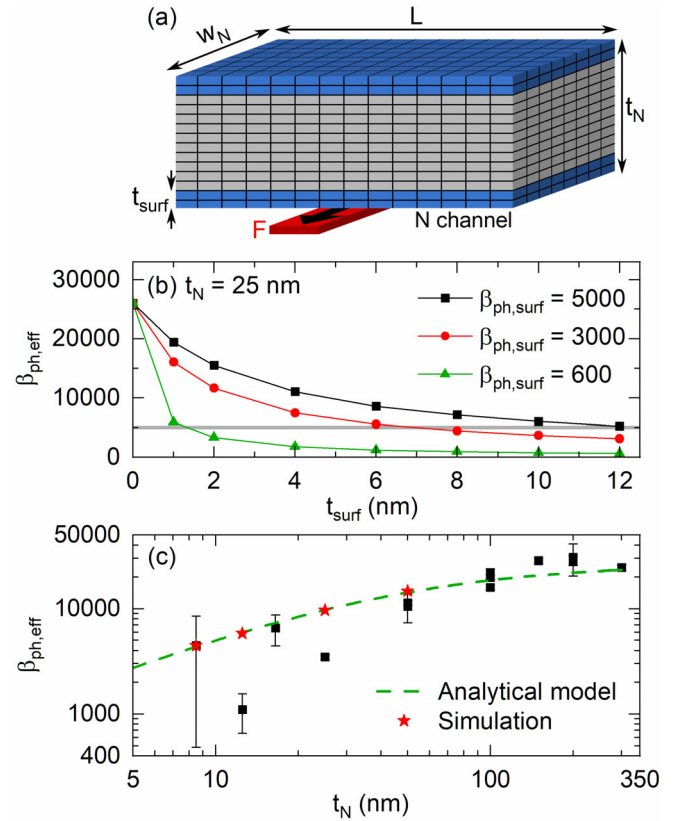

FIG. 4. (a) Numerical simulation schematic. (b) Simulated $\beta_{ph,eff}$ vs t_{surf} for $t_N = 25$ nm, for $\beta_{ph,surf}$ of 5000, 3000, and 600. (c) $\beta_{ph,eff}$ vs t_N ($\log_{10}$-$\log_{10}$ scale) from experiment (black points), Eq. (2) with $\beta_{ph,surf} = 600$, $t_{surf} = 0.5$ nm (green dashed line), and simulations with the same parameters (red points).

0.5 nm of the surface or interface can reproduce the data, with no need to invoke, e.g., enhanced spin relaxation at grain boundaries.

These conclusions are reinforced by simulations. As in prior work, we employ 3D Monte Carlo simulations [45], numerically solving the spin-diffusion equation for the geometry in Fig. 4(a). Details are provided in Ref. [45] and Supplemental Material, Sec. E [37], but, briefly, spins are injected from the F (red) into the Al channel of length $L_N = 10\lambda_N$, width $w_N = 160$ nm, and thickness t_N. The channel is broken into cells of $(\lambda_N/3) \times 40 \times 0.5$ nm^3, the spin relaxation rate in each cell being $\tau_s^{-1} = \tau_{s,def}^{-1} + \tau_{s,ph,j}^{-1}$. $\tau_{s,def}^{-1}$ is fixed from experiment [Fig. 3(a)] and $\tau_{s,ph,j}^{-1} = \beta_{ph,j}^{-1}\tau_{e,ph}^{-1}$, assigning $\beta_{ph,bulk} = 26\,000$ in the interior (gray) cells and a distinct $\beta_{ph,surf}$ in the surface or interface (blue) cells. The model is then iterated to find the steady-state spin polarization profile [45] and thus $\beta_{ph,eff} = \tau_{e,ph}^{-1}/\tau_{s,ph,eff}^{-1}$. Figure 4(b) shows the resulting $\beta_{ph,eff}(t_{surf})$ at an illustrative $t_N = 25$ nm, for $\beta_{ph,surf} = 5000$, 3000, and 600. Reproducing the experimental $\beta_{ph} = 5000$ at this t_N (horizontal gray line) requires unphysically large t_{surf} at large $\beta_{ph,surf}$, but only $t_{surf} \approx 1$ nm when $\beta_{ph,surf} = 600$. A full t_N

dependence is shown in Fig. 4(c), which plots $\beta_{ph,surf}$ ($\log_{10}$-$\log_{10}$ scale) from experiment (black points), Eq. (2) (green line), and simulation (red points), the latter two with $t_{surf} = 0.5$ nm and $\beta_{ph,surf} = 600$. Analytical and numerical results coincide, validating Eq. (2), and displaying good agreement with experiment. We thus conclude that the finite-size effect in $\beta_{ph}(t_N)$ [Figs. 3(c) and 4(c)] can be quantitatively understood in terms of efficient phonon-induced spin relaxation (low β_{ph}) within ~1 nm of the Al surface or interface.

The EY expectation that $\beta = (\Delta E / \lambda_{SO})^2$ suggests several potential contributors to reduced β_{ph} at surfaces or interfaces. First, and most importantly, λ_{SO} is well known to be enhanced under dimensional confinement and at surfaces or interfaces, the accompanying inversion symmetry breaking in films, 2D materials, and heterostructures leading to Rashba effects, Dzyaloshinskii-Moriya interactions, skyrmion formation, etc. [1–3]. Increased λ_{SO} therefore likely plays a significant role in rendering $\beta_{ph,surf} \ll \beta_{ph,bulk}$; in essence, phonon scattering near surfaces or interfaces occurs in environments with λ_{SO} enhanced over bulk, lowering β_{ph}. We emphasize that while the intrinsic λ_{SO} in Al is weak, EY spin relaxation *via* hot spots is extremely sensitive to λ_{SO}, and any enhancement of it, such as at the surfaces or interfaces deduced here. Second, it has recently been reported that inversion symmetry breaking at surfaces or interfaces can add D'yakanov-Perel' (DP) contributions to spin relaxation in thin metal films [56]. While this is more likely in higher Z metals [57], and may manifest through β_{def} rather than β_{ph}, future work exploring this in Al would be worthwhile. Third, surface or interface phonons with character distinct from the bulk could play a role, as in certain transport phenomena in metallic films [51]. Modified electronic structure could also contribute both surface or interface electronic and phononic effects potentially reducing ΔE, and thus β_{ph}. Future theoretical work is needed to assess the relative importance of these effects.

Finally, we emphasize that our findings may also be relevant beyond metals. EY spin relaxation is important in graphene, for example (where DP is also active) [58–60], which exists in a limit where surface or interface effects are anticipated, and enhanced β_{ph} may be the norm. In addition, the general approach in this Letter could also be powerful in 2D spin transport. Specifically, thickness tuning is used here to vary τ_e^{-1} and τ_s^{-1} (Fig. S3 [37]), combined with T-dependent analysis (e.g., Fig. 3) to separate phonon- and defect-induced contributions to τ_s^{-1} and thus determine β_{ph} and β_{def}. Related parametric tuning could be employed in graphene and other 2D materials, varying τ_e^{-1} and τ_s^{-1} via gate voltage [58,59], impurity adsorption [60], etc., then utilizing differing expected dependencies for EY and DP mechanisms to separate their contributions.

In summary, we have presented a detailed picture of phonon-induced EY spin relaxation in the model light metal Al, spanning a previously unexplored thickness range (8.5–300 nm). An unanticipated finite size effect emerges, where the EY "constant" for phonon scattering decreases over tenfold below ~100 nm. Based on analytical and numerical modeling, this was understood in terms of a reduced EY constant (enhanced phonon-induced spin relaxation) within ~1 nm of the surface or interface, implicating enhanced surface or interface spin-orbit coupling and posing well-defined challenges to theory.

*Corresponding author.
leighton@umn.edu

[1] F. Hellman *et al.*, Interface-induced phenomena in magnetism, Rev. Mod. Phys. **89**, 025006 (2017).

[2] A. Hirohata, K. Yamada, Y. Nakatani, I.-L. Prejbeanu, B. Diény, P. Pirro, and B. Hillebrands, Review on spintronics: Principles and device applications, J. Magn. Magn. Mater. **509**, 166711 (2020).

[3] *Handbook of Spin Transport and Magnetism*, edited by E. Tsymbal and I. Žutić, (CRC Press, Boca Raton, 2011).

[4] A. Brataas, A. D. Kent, and H. Ohno, Current-induced torques in magnetic materials, Nat. Mater. **11**, 372 (2012).

[5] R. J. Elliott, Theory of the effect of spin-orbit coupling on magnetic resonance in some semiconductors, Phys. Rev. **96**, 266 (1954).

[6] Y. Yafet, *g Factors, and Spin-Lattice Relaxation of Conduction Electrons, in Solid State Physics*, edited by F. Seitz and D. Turnbull, Vol. 14 (Academic Press, New York, 1963), pp. 1–98.

[7] F. Beuneu and P. Monod, The Elliott relation in pure metals, Phys. Rev. B **18**, 2422 (1978).

[8] J. Fabian and S. Das Sarma, Spin relaxation of conduction electrons, J. Vac. Sci. Technol. B **17**, 1708 (1999).

[9] S. Rakheja, S. C. Chang, and A. Naeemi, Impact of dimensional scaling and size effects on spin transport in copper and aluminum interconnects, IEEE Trans. Electron Devices **60**, 3913 (2013).

[10] H. Idzuchi, Y. Fukuma, and Y. Otani, Spin transport in nonmagnetic nano-structures induced by non-local spin injection, Physica (Amsterdam) **E68**, 239 (2015).

[11] F. J. Jedema, M. S. Nijboer, A. T. Filip, and B. J. van Wees, Spin injection and spin accumulation in all-metal mesoscopic spin valves, Phys. Rev. B **67**, 085319 (2003).

[12] J. D. Watts, L. O'Brien, J. S. Jeong, K. A. Mkhoyan, P. A. Crowell, and C. Leighton, Magnetic impurities as the origin of the variability in spin relaxation rates in Cu-based spin transport devices, Phys. Rev. Mater. **3,** 124409 (2019).

[13] M. Johnson and R. H. Silsbee, Interfacial Charge-Spin Coupling: Injection and Detection of Spin Magnetization in Metals, Phys. Rev. Lett. **55,** 1790 (1985).

[14] F. J. Jedema, A. T. Filip, and B. J. van Wees, Electrical Spin Injection and Accumulation at Room Temperature in an All-Metal Mesoscopic Spin Valve, Nature **410,** 345 (2001).

[15] S. Takahashi and S. Maekawa, Spin injection and detection in magnetic nanostructures, Phys. Rev. B **67,** 052409 (2003).

[16] G. Mihajlović, J. E. Pearson, S. D. Bader, and A. Hoffmann, Surface Spin Flip Probability of Mesoscopic Ag Wires, Phys. Rev. Lett. **104,** 237202 (2010).

[17] M. Erekhinsky, A. Sharoni, F. Casanova, and I. K. Schuller, Surface enhanced spin-flip scattering in lateral spin valves, Appl. Phys. Lett. **96,** 022513 (2010).

[18] A. J. Wright, M. J. Erickson, D. Bromley, P. A. Crowell, C. Leighton, and L. O'Brien, Origin of the magnetic field enhancement of the spin signal in metallic nonlocal spin transport devices, Phys. Rev. B **104,** 014423 (2021).

[19] Y. Cai, C. Qin, F. Kandaz, X. Shen, C. Zhou, M. Jia, Y. Luo, Y. Wu, and Y. Ji, Quantifying spin relaxation in mesoscopic Cu channels via a multitude of nonlocal spin valves, Phys. Rev. B **100,** 144419 (2019).

[20] J. T. Batley, M. C. Rosamond, M. Ali, E. H. Linfield, G. Burnell, and B. J. Hickey, Spin relaxation through Kondo scattering in Cu/Py lateral spin valves, Phys. Rev. B **92,** 220420(R) (2015).

[21] S. Karube, H. Idzuchi, K. Kondou, Y. Fukuma, and Y. Otani, Spin relaxation characteristics in Ag nanowire covered with various oxides, Appl. Phys. Lett. **107,** 122406 (2015).

[22] E. Villamor, M. Isasa, L. E. Hueso, and F. Casanova, Contribution of defects to the spin relaxation in copper nanowires, Phys. Rev. B **87,** 094417 (2013).

[23] H. Idzuchi, Y. Fukuma, L. Wang, and Y. Otani, Spin relaxation mechanism in silver nanowires covered with MgO protection layer, Appl. Phys. Lett. **101,** 022415 (2012).

[24] L. O'Brien, M. J. Erickson, D. Spivak, H. Ambaye, R. J. Goyette, V. Lauter, P. A. Crowell, and C. Leighton, Kondo physics in non-local metallic spin transport devices, Nat. Commun. **5,** 3927 (2014).

[25] K.-W. Kim, L. O'Brien, P. A. Crowell, C. Leighton, and M. D. Stiles, Theory of Kondo suppression of spin polarization in nonlocal spin valves, Phys. Rev. B **95,** 104404 (2017).

[26] L. O'Brien, D. Spivak, J. S. Jeong, K. A. Mkhoyan, P. A. Crowell, and C. Leighton, Interdiffusion-controlled Kondo suppression of injection efficiency in metallic nonlocal spin valves, Phys. Rev. B **93,** 014413 (2016).

[27] J. D. Watts, J. S. Jeong, L. O'Brien, K. A. Mkhoyan, P. A. Crowell, and C. Leighton, Room temperature spin Kondo effect and intermixing in Co/Cu non-local spin valves, Appl. Phys. Lett. **110,** 222407 (2017).

[28] P. W. Anderson, Localized magnetic states in metals, Phys. Rev. **124,** 41 (1961).

[29] P. Monod and F. Beuneu, Conduction-electron spin flip by phonons in metals: Analysis of experimental data, Phys. Rev. B **19,** 911 (1979).

[30] J. Fabian and S. Das Sarma, Spin Relaxation of Conduction Electrons in Polyvalent Metals: Theory and a Realistic Calculation, Phys. Rev. Lett. **81,** 5624 (1998).

[31] J. Fabian and S. Das Sarma, Phonon-Induced Spin Relaxation of Conduction Electrons in Aluminum, Phys. Rev. Lett. **83,** 1211 (1999).

[32] F. J. Jedema, H. B. Heersche, A. T. Filip, J. J. A. Baselmans, and B. J. van Wees, Electrical detection of spin precession in a metallic mesoscopic spin valve, Nature (London) **416,** 713 (2002).

[33] D. Lubzens and S. Schultz, Observation of an Anomalous Frequency Dependence of the Conduction-Electron Spin Resonance in Al, Phys. Rev. Lett. **36,** 1104 (1976).

[34] Y. K. Takahashi, S. Kasai, S. Hirayama, S. Mitani, and K. Hono, All-metallic lateral spin valves using $Co_2Fe(Ge_{0.5}Ga_{0.5})$ Heusler alloy with a large spin signal, Appl. Phys. Lett. **100,** 052405 (2012).

[35] M. Yamada, D. Sato, N. Yoshida, M. Sato, K. Meguro, and S. Ogawa, Scalability of spin accumulation sensor, IEEE Trans. Magn. **49,** 713 (2013).

[36] T. Nakatani, Z. Gao, and K. Hono, Read sensor technology for ultrahigh density magnetic recording, MRS Bull. **43,** 106 (2018).

[37] See Supplemental Material at http://link.aps.org/supplemental/10.1103/PhysRevLett.128.207201 for details on fabrication and other analysis, which includes Refs. [38,39].

[38] J. Bass, W. P. Pratt, and P. A. Schroeder, The temperature-dependent electrical resistivities of the alkali metals, Rev. Mod. Phys. **62,** 645 (1990).

[39] A. Bid, A. Bora, and A. K. Raychaudhuri, Temperature dependence of the resistance of metallic nanowires of diameter ≥ 15 nm: Applicability of Bloch-Grüneisen theorem, Phys. Rev. B **74,** 035426 (2006).

[40] F. L. Bakker, A. Slachter, J. P. Adam, and B. J. Van Wees, Interplay of Peltier and Seebeck Effects in Nanoscale Nonlocal Spin Valves, Phys. Rev. Lett. **105,** 136601 (2010).

[41] T. Sun, B. Yao, A. P. Warren, K. Barmak, M. F. Toney, R. E. Peale, and K. R. Coffey, Surface and grain-boundary scattering in nanometric Cu films, Phys. Rev. B **81,** 155454 (2010).

[42] A. F. Mayadas and M. Shatzkes, Electrical-resistivity model for polycrystalline films: The case of arbitrary reflection at external surfaces, Phys. Rev. B **1,** 1382 (1970).

[43] J. D. Watts, J. T. Batley, N. A. Rabideau, J. P. Hoch, L. O'Brien, P. A. Crowell, and C. Leighton (unpublished).

[44] T. Valet and A. Fert, Theory of the perpendicular magneto-resistance in magnetic multilayers, Phys. Rev. B **48,** 7099 (1993).

[45] L. O'Brien, D. Spivak, N. Krueger, T. A. Peterson, M. J. Erickson, B. Bolon, C. C. Geppert, C. Leighton, and P. A. Crowell, Observation and modelling of ferromagnetic contact-induced spin relaxation in hanle spin precession measurements, Phys. Rev. B **94,** 094431 (2016).

[46] J. Bass and W. P. Pratt, Spin-diffusion lengths in metals and alloys, and spin-flipping at metal/metal interfaces: An

experimentalist's critical review, J. Phys. Condens. Matter **19**, 183201 (2007).

[47] N. W. Ashcroft and N. D. Mermin, *Solid State Physics* (Brooks/Cole, New York, 1976).

[48] F. Beuneu and P. Monod, Conduction-electron spin resonance in cold-worked Al, Cu, and Ag: The spin-flip cross section of dislocations, Phys. Rev. B **13**, 3424 (1976).

[49] Note that Ref [11] uses $1.55 \times 10^6 \ \mathrm{ms}^{-1}$ for Al Fermi velocity, while we use $2.03 \times 10^6 \ \mathrm{ms}^{-1}$ (the free electron model value). Thus the reported EY constants differ by a factor of $(1.55/2.03)^2$.

[50] W. Ma, X. Zhang, and K. Takahashi, Electrical properties and reduced Debye temperature of polycrystalline thin gold films, J. Phys. D **43** (2010).

[51] S. Kim, H. Suhl, and I. K. Schuller, Surface Phonon Scattering in the Electrical Resistivity on Co/Ni Superlattices, Phys. Rev. Lett. **78**, 322 (1997).

[52] D. Josell, S. H. Brongersma, and Z. Tőkei, Size-dependent resistivity in nanoscale interconnects, Annu. Rev. Mater. Res. **39**, 231 (2009).

[53] G. Benedek, M. Bernasconi, V. Chis, E. Chulkov, P. M. Echenique, B. Hellsing, and J. Peter Toennies, Theory of surface phonons at metal surfaces: Recent advances, J. Phys. Condens. Matter **22**, 084020 (2010).

[54] J. R. Rumble, *CRC Handbook of Chemistry and Physics*, 98th ed. (Boca Raton, FL, 2017).

[55] R. Stedman and G. Nilsson, Dispersion relations for phonons in Aluminum at 80 and 300 °K, Phys. Rev. **145**, 492 (1966).

[56] N. H. Long, P. Mavropoulos, D. S. G. Bauer, B. Zimmermann, Y. Mokrousov, and S. Blügel, Strong spin-orbit fields and Dyakonov-Perel spin dephasing in supported metallic films, Phys. Rev. B **94**, 180406(R) (2016).

[57] C. T. Boone, J. M. Shaw, H. T. Nembach, and T. J. Silva, Spin-scattering rates in metallic thin films measured by ferromagnetic resonance damping enhanced by spin-pumping, J. Appl. Phys. **117**, 223910 (2015).

[58] P. J. Zomer, M. H. D. Guimarães, N. Tombros, and B. J. Van Wees, Long-distance spin transport in high-mobility graphene on hexagonal boron nitride, Phys. Rev. B **86**, 161416(R) (2012).

[59] G. Stecklein, P. A. Crowell, J. Li, Y. Anugrah, Q. Su, and S. J. Koester, Contact-Induced Spin Relaxation in Graphene Nonlocal Spin Valves, Phys. Rev. Applied **6**, 054015 (2016).

[60] K. Pi, W. Han, K. M. McCreary, A. G. Swartz, Y. Li, and R. K. Kawakami, Manipulation of Spin Transport in Graphene by Surface Chemical Doping, Phys. Rev. Lett. **104**, 187201 (2010).